








High-energy and low-cost membrane-free chlorine flow battery

Singyuk Hou ^{1,5}, Long Chen ^{1,2,5}✉, Xiulin Fan^{1,5}, Xiaotong Fan³, Xiao Ji ¹, Boyu Wang¹, Chunyu Cui¹, Ji Chen¹, Chongyin Yang ¹, Wei Wang ⁴, Chunzhong Li ² & Chunsheng Wang ¹✉

Grid-scale energy storage is essential for reliable electricity transmission and renewable energy integration. Redox flow batteries (RFB) provide affordable and scalable solutions for stationary energy storage. However, most of the current RFB chemistries are based on expensive transition metal ions or synthetic organics. Here, we report a reversible chlorine redox flow battery starting from the electrolysis of aqueous NaCl electrolyte and the as-produced Cl₂ is extracted and stored in the carbon tetrachloride (CCl₄) or mineral spirit flow. The immiscibility between the CCl₄ or mineral spirit and NaCl electrolyte enables a membrane-free design with an energy efficiency of >91% at 10 mA/cm² and an energy density of 125.7 Wh/L. The chlorine flow battery can meet the stringent price and reliability target for stationary energy storage with the inherently low-cost active materials (~\$5/kWh) and the highly reversible Cl₂/Cl⁻ redox reaction.

¹Department of Chemical and Biomolecular Engineering, University of Maryland, College Park, MD, USA. ²Department of Chemical Engineering, East China University of Science and Technology, Shanghai, China. ³School of Materials Science and Engineering, East China University of Science and Technology, Shanghai, China. ⁴Energy & Environment Directorate, Pacific Northwest National Laboratory, Richland, WA, USA. ⁵These authors contributed equally: Singyuk Hou, Long Chen, Xiulin Fan. ✉email: longchen@ecust.edu.cn; cswang@umd.edu

Integrating renewable energy, such as solar and wind power, is essential to reducing carbon emissions for sustainable development. However, large-scale utilization is hindered by the intermittence and uneven distribution of these power sources^{1–3}. Implementation of grid-scale energy storage is essential to mitigate the mismatch between electricity production and consumption⁴. Different technologies are developed for this purpose, including supercapacitors, sodium–sulfur batteries, pump hydro, flywheels, and superconducting magnetic energy⁵. Redox flow battery (RFB) is considered one of the most attractive energy storage systems for large-scale applications due to the lower capital cost, higher energy conversion efficiency, and facile modularity^{6,7}. The cores of flow cells are the circulating electrolytes that carry the redox-active materials for energy storage and release.

Currently, the all-vanadium RFB is the most researched and developed RFB chemistry; however, the market adoption of this system has been hampered by high-cost chemicals (material cost close to 60% of the overall system cost⁸ and low energy density. Although aqueous soluble organic redox species offer a potential option for low-cost materials^{9–15}, the synthetic processes required to customize the molecular structure for high solubility and optimal potential will again limit the material cost and availability^{6,16–18}. Also, they rely on the costly ion-permeable membranes to reduce cross-over, further increasing capital and maintenance costs¹⁹.

Recently, polymer redox couples were developed to circumvent ion-permeable membranes²⁰, and the semi-solid Li-ion (suspensions of Li-ion battery active materials in nonaqueous electrolytes) systems have been explored for higher energy density and efficiency. However, high viscosity, lower peak power operation time, and high material cost emerged with these systems^{4,21,22}.

To meet the needs of RFB chemistries with the naturally abundant and low-cost redox-active materials, we report a new RFB system that capitalizes the electrolysis of saltwater or aqueous NaCl electrolyte using the Cl₂/Cl[−] redox couple as the active material for the positive electrode. The Cl₂/Cl[−] has a theoretical capacity of 755 mAh/g, more than two times that of vanadium oxides (VO₂⁺/VO²⁺, 226 mAh/g) used in current RFBs. Cl₂/Cl[−] redox chemistry is a fast single-electron transferred reaction with an activation energy of 35.5 kJ/mol^{23,24}, which is comparable to or even smaller than that of VO₂⁺/VO²⁺²⁵, thus is suitable for high power applications. In addition, sodium chloride is one of the cheapest commodities available due to the abundant source in seawater and large-scale production (~\$40 per metric ton)^{26,27}. These features enable Cl₂/Cl[−] redox reaction to be a promising candidate for RFB.

Rarely heard in the battery history is that Cl₂/Cl[−] redox couple was used in the RFB to power the first fully controlled airship La France in 1884²⁸. The Cl₂/Cl[−] based batteries are often typified by low Coulombic efficiency (CE) of 40–70%^{29–33} due to Cl₂ dissolution in the electrolytes and large voltage hysteresis (0.7 V at 32 mA/cm²) due to non-wettability between electrolytes and electrodes^{34,35}, which limits the energy efficiency to around 60%. Graphite was reported as chlorine storage host via intercalation³⁶. However, the instability of Cl₂ intercalated graphite at room temperature results in low storage capacity (35–40 mAh/g) and limited cycle life. After that, no other materials with appropriate stability, storage capacity, and reaction kinetics have been reported to enable reversible Cl₂ electrochemical reaction.

Our objective is to develop a new RFB with the highly reversible Cl₂/Cl[−] redox species through electrolyzing the saturated NaCl aqueous electrolyte (NaCl/H₂O) and storing the as-produced Cl₂ in water-immiscible organic phases such as carbon tetrachloride (CCl₄) or mineral spirits. These organic phases provide several desirable properties: (1) Cl₂ in CCl₄ (Cl₂-CCl₄) delivers a

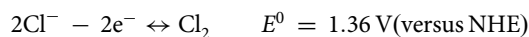
volumetric capacity of 97 Ah/L due to high solubility of Cl₂ in CCl₄ (0.184 mole/mole CCl₄³⁷, which is a 2 to 4 times improvement over the current vanadium-based catholyte (22.6–43.1 Ah/L³⁸); (2) The Cl₂-CCl₄ is immiscible to NaCl/H₂O, thus requires no membrane to prevent cross-over, further reducing costs; (3) The Cl₂-CCl₄ has low and constant viscosity of 0.819 mPa.s, in contrast to high and varying viscosity of aqueous vanadium-based catholyte (1.4–3.2 mPa.s³⁹, thus is easy to flow; (4) Cl₂-CCl₄ can wet carbon porous electrodes easily, which significantly enhances the surface area for Cl₂ storage and reaction; (5) Cl₂ has high diffusivity in CCl₄, minimizing energy dissipation for mass transport.

Results

Storage and electrochemical performance of Cl₂-CCl₄. The Cl₂/Cl[−] redox reaction in NaCl/H₂O was evaluated in a concentric cell with RuO₂-TiO₂ coated porous carbon (RuO₂-TiO₂@C) as a working electrode, activated carbon as a counter electrode (Fig. S1), and Ag/AgCl as the reference electrode (Fig. 1A). The RuO₂-TiO₂ catalysts on porous carbon (Figs. S2, S3) are used to promote the oxidation kinetics of chloride^{40–43} (Fig. S4). CCl₄ was pumped through the working electrode, and the NaCl/H₂O through the interstitial space between the working and counter electrodes to ensure adequate Cl[−] supply. While CCl₄ and NaCl/H₂O entered the RuO₂-TiO₂@C electrode as separate flows, they both wet the carbon electrode, demonstrated by <90° contact angles (CAs) on a graphite plate electrode (Fig. 1B, C). And the two liquids take up 66.2% and 33.8% of the void volume in the RuO₂-TiO₂@C electrode, respectively (see the determination of percentage volume in Supplementary Note 1). The ion-permeable membrane used in traditional RFBs to prevent cross-contamination^{15,16,44–46} is not required here since the Cl₂-CCl₄ and NaCl/H₂O are phase separated.

During charge, the Cl₂ was generated from oxidizing the Cl[−] in the RuO₂-TiO₂@C electrode. The reaction shows a constant potential at 1.2 V versus Ag/AgCl reference electrode [1.36 V versus normal hydrogen electrode (NHE)]. During discharge, the Cl₂ in CCl₄ was reduced to Cl[−] in the working electrode and entered the NaCl/H₂O (see the formulation for positive electrode reaction). The presence of CCl₄ flow significantly enhances the coulombic efficiency (CE) from 8 to 97% (Fig. 1D). Because the solubility of Cl₂ in CCl₄ is three orders of magnitude higher than that in NaCl/H₂O (0.184 mole/mole CCl₄ versus 0.0005 mole/mole NaCl/H₂O³⁸) (Fig. 1E), the Cl₂ generated during the charging process can be stored in CCl₄, which prevents Cl₂ diffusion into NaCl/H₂O as supported by Raman spectroscopy (Fig. S5) and the positive Gibbs free energy to transfer Cl₂ from CCl₄ to NaCl/H₂O (Fig. S6). When 6.0 mL CCl₄ was used, a maximum reversible capacity for Cl₂/Cl[−] conversion is 600 mAh (Fig. S7), rendering the capacity of 97 Ah/L for the Cl₂-CCl₄.

Positive electrode reaction.



The Cl₂-CCl₄ positive electrode has a low and almost consistent viscosity. When the concentration of Cl₂ increases from 0 to 0.184 mole/mole CCl₄ (saturation), the viscosity even slightly decreases from 0.894 to 0.819 mPa.s (Fig. 1F) in accord to Eyring's absolute reaction rate theory for gas–liquid mixtures^{47,48}. On the other hand, the viscosity of common catholyte could increase by several or even dozen times as the concentration of solute increases⁴⁹. The low viscosity of Cl₂-CCl₄ reduces the pumping loss⁴⁰, and the steady viscosity minimizes the

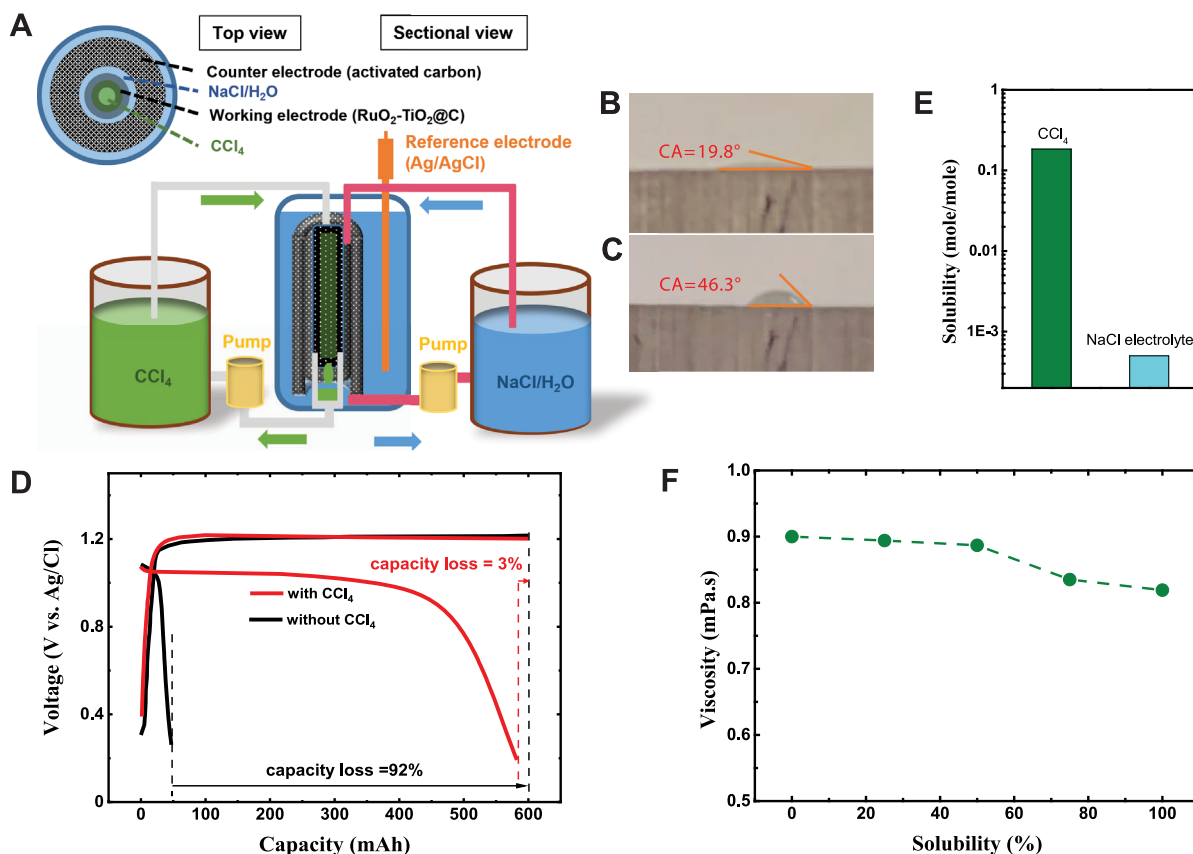


Fig. 1 Electrochemical performance and physical properties of $\text{Cl}_2\text{-CCl}_4$. **A** Schematic of the three-electrode cell. Inset shows the cylindrical structure of the cell from the top view, in which the inner diameter of the $\text{RuO}_2\text{-TiO}_2\text{@C}$ working electrode is 2.0 mm, the thickness of the $\text{RuO}_2\text{-TiO}_2\text{@C}$ electrode is 1.0 mm, the distance between the working and counter electrode is 3.0 mm and the thickness of the counter electrode is 3.0 mm. The height is 2.0 cm, and the volume capacity of the cell is around 2.0 mL. The total volumes of the CCl_4 reservoir and the $\text{NaCl}/\text{H}_2\text{O}$ reservoir are 6.0 mL and 2.0 mL, respectively. **B** CA of CCl_4 on graphite plate electrode. **C** CA of $\text{NaCl}/\text{H}_2\text{O}$ on graphite plate electrode. **D** Galvanostatic charge and discharge profiles of $\text{Cl}_2\text{-CCl}_4$ (red) and Cl_2 without CCl_4 (black) at the current density of $20 \text{ mA}/\text{cm}^2$. Both cells ran with constant charge capacity of 600 mAh at Q_{aq} (flow rate of $\text{NaCl}/\text{H}_2\text{O}$) = $0.02 \text{ mL}/\text{s}$ and Q_{org} (flow rate of CCl_4) = $0.002 \text{ mL}/\text{s}$. The differences between discharge and charge capacity are labeled as percentage capacity loss. **E** The solubility of Cl_2 in CCl_4 and $\text{NaCl}/\text{H}_2\text{O}$. **F** The viscosities of $\text{Cl}_2\text{-CCl}_4$ with different concentrations of Cl_2 (100% refers to saturation).

volumetric transfer between catholyte and anolyte at different SOC_s^{50,51}.

Full chlorine flow battery (CFB). To fabricate a full CFB, the activated carbon counter electrode was replaced by $\text{NaTi}_2(\text{PO}_4)_3$ negative electrode (Fig. 2A). $\text{NaTi}_2(\text{PO}_4)_3$ (Figs. S8, S9) was chosen as the negative electrode due to low potential (-0.5 V versus NHE), rapid and reversible Na-ion insertion/extraction in $\text{NaCl}/\text{H}_2\text{O}$ demonstrated by the symmetric anodic and cathodic peaks with 60 mV separation in the cyclic voltammetry (negative electrode reaction and Fig. S10A)⁵². The $\text{NaTi}_2(\text{PO}_4)_3$ shows a 65% capacity retention even at the C-rate of 315 C (1 C = fully discharge/charge within 1 hour, Fig. S10) and long cycle life of 1000 cycles (Fig. S11).

Negative electrode reaction.



While the overpotentials enhanced (orange dash lines in Fig. 2B, C) as the current density increased, the discharge capacities did not vary (Fig. 2B, C), which could be attributed to the large reaction surface area endowed by the wetting between carbon electrode and $\text{Cl}_2\text{-CCl}_4$ (Fig. 1B, C). Fig. 2D demonstrates cell voltage efficiency (defined as the potential ratio of discharge

to charge) of 93.6% at $10 \text{ mA}/\text{cm}^2$ and $\sim 77\%$ at $100 \text{ mA}/\text{cm}^2$. The multiplication of discharge capacity and voltage gives the cell power density that peaks at $325 \text{ mW}/\text{cm}^2$ when operated at $350 \text{ mA}/\text{cm}^2$ (Fig. 2E). It is worth noting that polarizations for discharge are more significant than those for discharge (Fig. 2B, C). In the CFB, overpotentials are caused by redox reactions and concentration gradient. Since the symmetric factors for Cl^-/Cl_2 redox reactions are equal^{17,25}, the overpotentials needed to drive the reduction and oxidation reaction are the same, the different overpotentials for charge and discharge observed here could only be attributed to the concentration gradient.

A steady-state model was developed to understand the species distribution and controlling steps in the CFB. The Nernst-Planck equation was applied to the porous $\text{RuO}_2\text{-TiO}_2\text{@C}$ electrode (cell width = 0–1.0 mm in Fig. 2A), and $\text{NaCl}/\text{H}_2\text{O}$ (cell width = 1.0–4.0 mm in Fig. 2A), Fick's equation was applied to the $\text{Cl}_2\text{-CCl}_4$ phase (cell width = –2.0–0 mm in Fig. 2A). The negative electrode was involved implicitly at the boundary of the $\text{NaCl}/\text{H}_2\text{O}$ (cell width = 4.0 mm in Fig. 2A) (see model description and Tables S1–S4 in Supplementary Note 1). The model was validated by the agreement between the simulated and experimental cell voltages (black lines and dots in Fig. 3A, B, experimental potential retrieved from Fig. 2B, C) at the same flow rates and current densities.

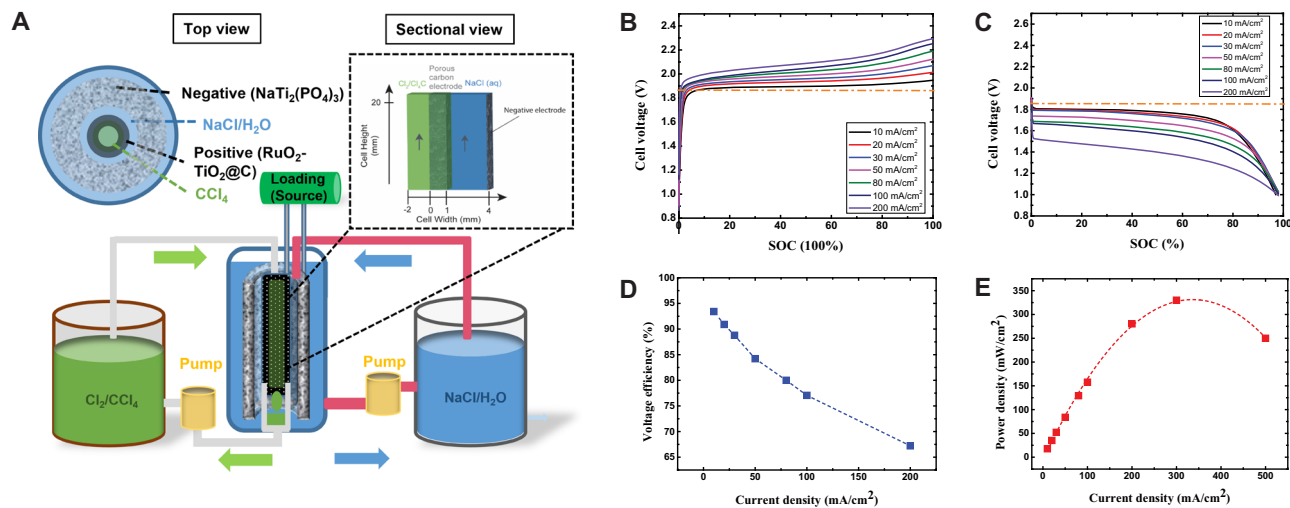


Fig. 2 Schematic and electrochemical performance of chlorine flow battery (CFB). **A** Schematic of the CFB, the inner diameter of the tube containing CCl_4 and $\text{RuO}_2\text{-TiO}_2\text{@C}$ electrode is 2.0 mm, the thickness of the $\text{RuO}_2\text{-TiO}_2\text{@C}$ electrode is 1.0 mm, the distance between the working and counter electrode is 3.0 mm. The thickness of the counter electrode is 3.0 mm. The height of the cell is 2.0 cm, and the volume capacity of the cell is around 2.0 mL. The total volumes of the CCl_4 reservoir and the $\text{NaCl}/\text{H}_2\text{O}$ reservoir are 6.0 mL and 2.0 mL, respectively. $Q_{\text{aq}} = 0.02 \text{ mL/s}$ and $Q_{\text{org}} = 0.002 \text{ mL/s}$. Galvanostatic charge **B** and discharge **C** profiles of the CFB at different current densities. The state of charge (SOC) of the battery is normalized to the maximum reversible capacity at 10 mA/cm^2 , in which 100% SOC represents charge to 600 mAh. **D** The voltage efficiencies of the CFB at different current densities. **E** The power densities of the CFB at different current densities.

The model was then used to visualize the species distribution in the $\text{NaCl}/\text{H}_2\text{O}$ and in $\text{Cl}_2\text{-CCl}_4$. During charge, the Cl^- in $\text{NaCl}/\text{H}_2\text{O}$ was consumed inside the porous carbon electrode (Fig. 3C) and limits the reaction kinetics; during discharge, Cl_2 in CCl_4 is consumed and limits the reaction kinetics. The Cl^- concentration gradients are more significant than the Cl_2 concentration gradient in the porous electrode for both charge and discharge (Fig. 3C, D), which is the result of a smaller diffusivity of Cl^- ($1.5 \times 10^{-5} \text{ cm}^2/\text{s}$ for Cl^- , $2.0 \times 10^{-5} \text{ cm}^2/\text{s}$ for Cl_2 in $\text{NaCl}/\text{H}_2\text{O}$ and $3 \times 10^{-5} \text{ cm}^2/\text{s}$ for Cl_2 in CCl_4 ^{53–55} and lower volume percentage of $\text{NaCl}/\text{H}_2\text{O}$ than CCl_4 in the porous carbon electrode. The distinct species that control charge and discharge kinetics thus generate the asymmetric charge and discharge overpotentials (Fig. 2B, C). Since Cl^- and Cl_2 are in different phases, increasing the flow rate of $\text{NaCl}/\text{H}_2\text{O}$ during charge and that of the $\text{Cl}_2\text{-CCl}_4$ during discharge enhance the mass transport of the limiting species accordingly, in which not only the overpotentials reduce, but the current density range allowing steady cell voltage extends (inset of Fig. 3A, B). At the highest flow rate examined, the voltage efficiency could be postulated to >93% at 20 mA/cm^2 .

The high voltage efficiency of the cell is attributed not only to the fast reaction kinetics but also the membrane-free configuration. The potential gradient in the $\text{NaCl}/\text{H}_2\text{O}$ was determined by the model (Fig. 4A, B), and the potential difference across the cell at half-cell height was plotted. The potential drop of $\sim 20 \text{ mV}$ at 10 mA/cm^2 and $\sim 250 \text{ mV}$ at 100 mA/cm^2 (Fig. 4C) are equivalent to proton transport but over 5 times smaller than Na^+ and K^+ transport in Nafion ion-permeable membranes in aqueous flow batteries with similar cell dimensions⁵⁶. Thus, removing the ion-selective membrane opens a range of chemistries to be investigated, as the charge carriers can be chosen arbitrarily.

The CFB demonstrates the round-trip energy efficiency of 91% (calculated by voltage efficiency \times Coulombic efficiency) at 10 mA/cm^2 and provides an energy density of 125.7 Wh/L (see Methods), which is among the highest of the flow battery systems reported in past 10 years (Table S5). It is worth noting that the $\text{Cl}_2\text{-CCl}_4$ is different from bromine used in flow batteries that faces the serious self-discharge due to the diffusion of Br_2 to the negative electrodes in the form of polybromide. When ion-

permeable membranes were used to decrease Br_2 cross-over, voltage efficiency was significantly limited by the transport of ions in the membrane, resulting in <80% energy efficiency in overall performance^{57–59}. Figure 5A, B show the measured cell voltage profile and stable round-trip cycling for this battery at 20 mA/cm^2 with a charge storage capacity of 600 mAh and the stable capacity retention for 500 cycles.

Discussion

In this study, CCl_4 was used as a proof of concept, it can be replaced by other liquids with high Cl_2 solubility and are immiscible with $\text{NaCl}/\text{H}_2\text{O}$. The candidates include heptane (chlorine solubility = 0.173 mole fraction at ambient temperature), octane (chlorine solubility = 0.168 mole fraction at ambient temperature), tetradecane (chlorine solubility = 0.254 mole fraction at ambient temperature)²⁹ and mineral spirit. Mineral spirit demonstrates good wettability ($\text{CA} = 9.1^\circ$) with carbon current collector (Fig. S12A), low viscosity ($1.24 \text{ mPa}\cdot\text{s}$), low toxicity, and is cheaper than CCl_4 ⁶⁰. When CCl_4 was replaced by mineral spirit in the CFB, a volumetric capacity of 91.6 Ah/L was delivered at 20°C (Fig. S12B).

The removal of the ion-permeable membrane also allows multivalent ions as charge carriers. When ZnCl_2 is added to the electrolyte, $\text{NaTi}_2(\text{PO}_4)_3$ can be replaced by zinc metal electrode, increasing the cell operating voltage to 1.9 V (Fig. S13).

Cost is one of the significant concerns to implementing flow batteries on a large scale for stationary energy storage. Considering that the ion-permeable membrane (mainly perfluorinated polymers) takes up more than 30% of the cost of flow batteries, significant cost reduction is expected with the membrane-free design²⁰. The total material cost for energy storage with the proposed CFB is estimated to be $\sim \$5/\text{kWh}$, which is the cheapest among all the current flow battery systems (Fig. 5C and Table S5). In addition, the RuO_2 catalyst for chlorine evolution reaction (CER) can also be replaced by tin, zinc, cobalt, and other cheap metal oxides partially³⁰. Therefore, the proposed CFB design leaves significant space to meet the stringent target of $\sim \$100/\text{kWh}$ for RFB applications⁶¹.

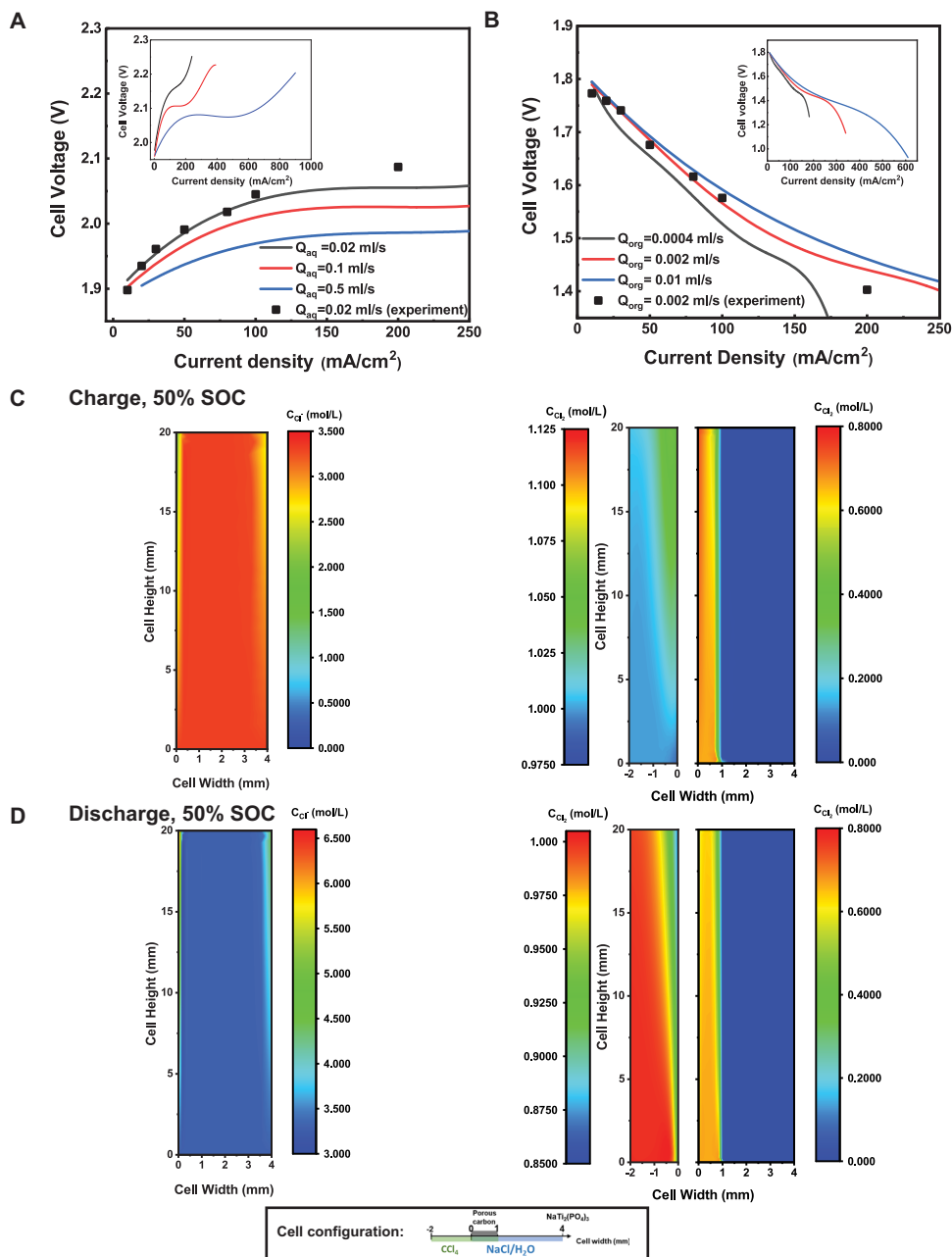


Fig. 3 Simulation of the CFB. A Steady-state potentials of CFB charged at 50% SOC with different Q_{aq} and $Q_{org} = 0.002$ mL/s, inset shows the whole current density range demonstrating steady charge potential. **B** Steady-state potentials of CFB discharged at 50% SOC with different Q_{org} and $Q_{aq} = 0.02$ mL/s, inset shows the whole current density range demonstrating steady discharge potential. **C** Distribution of Cl^- and Cl_2 in the CFB charged at 50% SOC and 50 mA/cm² with $Q_{aq} = 0.02$ mL/s and $Q_{org} = 0.002$ mL/s. **D** Distribution of Cl^- and Cl_2 in the CFB discharged at 50% SOC and 50 mA/cm² with $Q_{aq} = 0.02$ mL/s and $Q_{org} = 0.002$ mL/s. The position of Cl_2 - CCl_4 , $NaCl/H_2O$, porous RuO_2 - $TiO_2@C$ positive electrode and $NaTi_2(PO_4)_3$ negative electrode are labeled in the legend.

Cl_2 is a reactive chemical commodity used in paper, plastic, dye, textile, medicine, antiseptics, insecticide, solvent, and paint industries. Administration and engineering controls for storage and transport are available to confine the incident rate to 0.019% of total chlorine shipments between 2007 and 2017⁶². The Occupational Safety and Health Administration of the United States has set a permissible exposure limit at a time-weighted average of 0.1 ppm (0.68 mg/m³) for bromine, 0.05 mg/m³ for vanadium pentoxide dust, 0.1 ppm (0.4 mg/m³) for quinone, and 1.0 ppm (3 mg/m³) for chlorine⁶³. Thus, there is no apparent increase in chemical exposure risk when changing to chlorine redox reaction.

However, protections and cautions are still crucial. The CFB proposed here is a closed system in which the leakage of Cl_2 gas is minimized by the fluoropolymer gasket (see Supplementary Note 2 for evaluation of chlorine permeation). Strategies from the chloro-alkali industry can be applied to reduce the risk of exposure upon scaling up, such as external seal pipe, shutoff system, neutralization reagents (scrubber)⁶⁴, and sensing systems⁶⁵.

In summary, the CFB proposed has demonstrated several unique advantages over current flow battery systems, including higher energy density, higher round-trip energy efficiency, and significantly lower prices. The membrane-free design enables both anionic and cationic charge carriers for a RFB, thus

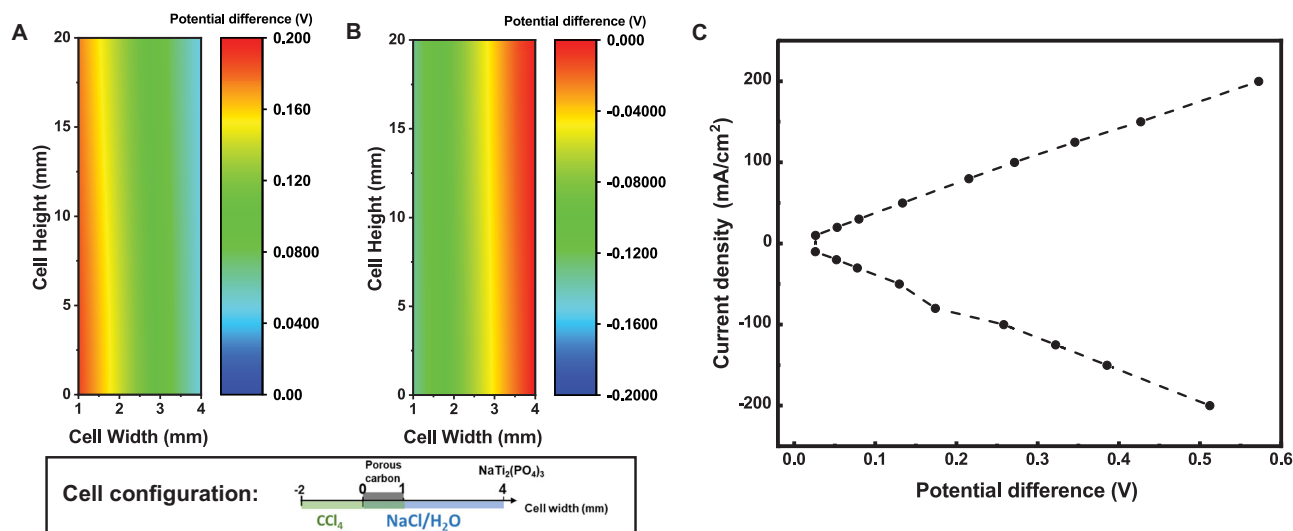


Fig. 4 Potential gradient in the electrolyte of CFB. A Potential distribution during charge and **B** during discharge at 50% SOC and 50 mA/cm². **C** The potential loss due to ion transport in the NaCl/H₂O at different current densities. In all cases $Q_{\text{aq}} = 0.02$ mL/s and $Q_{\text{org}} = 0.002$ mL/s. The positions of Cl₂-CCl₄, NaCl/H₂O, porous RuO₂-TiO₂@C positive electrode, and NaTi₂(PO₄)₃ negative electrode are labeled in the legend.

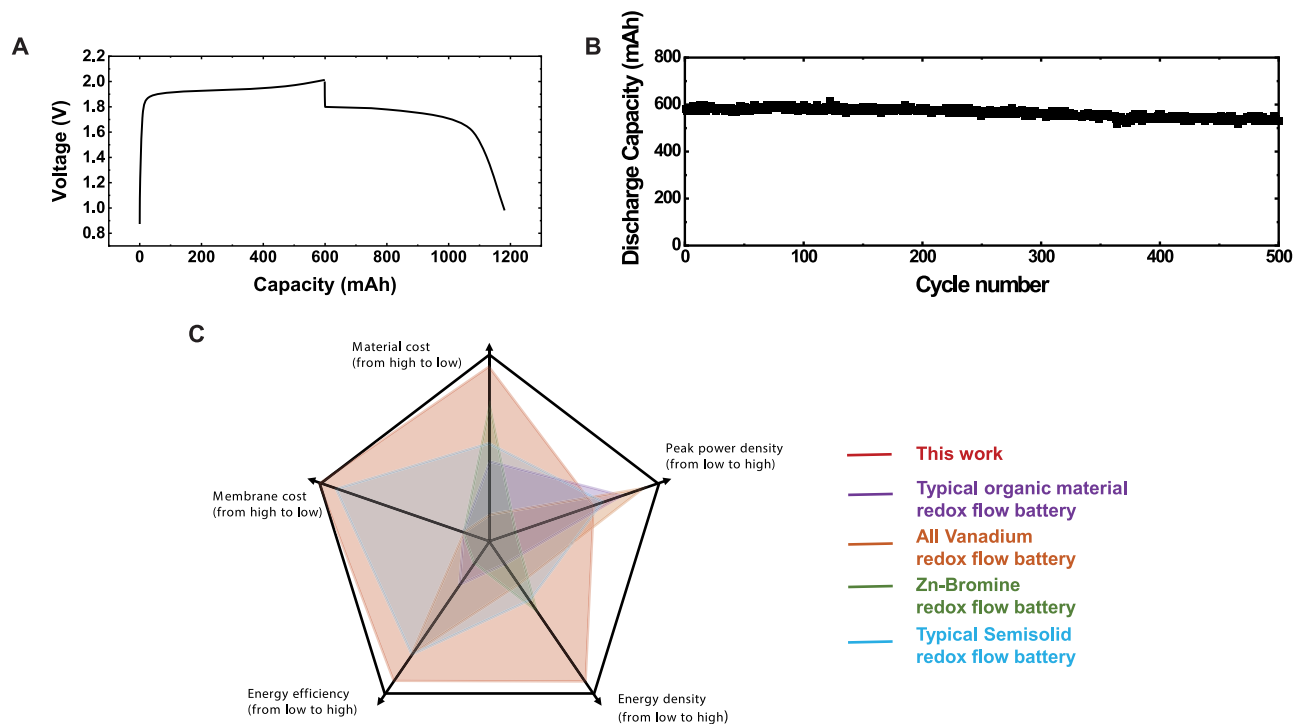


Fig. 5 Charge and discharge behavior of CFB and comparisons of the performance matrices to redox flow batteries reported in the past 10 years. A Cell voltage profiles during constant-current cycling and **B** cycle performance of CFB at 20 mA/cm², $Q_{\text{aq}} = 0.02$ mL/s and $Q_{\text{org}} = 0.002$ mL/s, and the charge capacity was set to be 600 mAh. The amount of CCl₄ is 6.0 mL, the size of the porous RuO₂-TiO₂@C electrode is 1.0 mm-thick and 2.0 cm² area. **C** The comparison of performance matrices among CFB, organic redox flow battery (anthraquinones as the anode material and ferricyanide as cathode material, ref. S24), all-vanadium redox flow battery (refs. S28, 29), Zn-Bromine redox flow battery (ref. S33), and semi-solid redox flow battery (Li as the anode and LiFePO₄ as cathode material ref. S34) (see details in Table S5).

expanding the material and chemistry space of the redox flow technologies.

Methods

Material synthesis. The activated carbon with RuO₂/TiO₂ particles was prepared by dissolving 0.69 mmol RuCl₃ and 1.622 mmol C₁₆H₃₆O₄Ti in 100 mL isopropanol, then adding 2.0 g activated carbon into the solution. The mixture was stirred for 2 hours, and then the isopropanol was evaporated at 90 °C. Finally, the products were annealed at 500 °C for 1 hour under ambient conditions.

The carbon-coated NaTi₂(PO₄)₃ was synthesized from 0.002475 mol Na₂CO₃, 0.01485 mol NH₄H₂PO₄, and 0.0099 mol TiO₂ in 100 mL of a 2.0 wt% poly-vinyl-alcohol (PVA) aqueous solution. The mixture was stirred at 80 °C until the water evaporated and white solids formed. The white solids were placed in a porcelain boat and heated at 900 °C for 10 hours with an increasing rate of 5 °C/min under an N₂ flow in a tube furnace. To improve the cycling stability and electronic conductivity, thermal vapor deposition (TVD) was employed to prepare carbon-coated NaTi₂(PO₄)₃ after calcination. The as-prepared powder was transferred into a reaction tube to make a fluid-bed layer for the reaction at 700 °C for 2 hours where a toluene vapor was carried by N₂ through the reaction tube at a flow rate of

1 L/min, followed by heat-treatment at 900 °C for 2 hours without toluene carrying gas to increase its electronic conductivity. The temperature increasing rate is 5.0 °C/min.

Electrode preparation and electrochemical measurements. The working electrode was fabricated by pressing a mixture of the active materials (porous carbon or carbon-coated $\text{NaTi}_2(\text{PO}_4)_3$), carbon black, and PTFE (polytetrafluoroethylene) binder at the weight ratio of 7:2:1 onto a titanium grid with a pressure of 10 MPa. The cyclic voltammograms (CV) were obtained using a three-electrode cell with an active carbon counter electrode and Ag/AgCl reference electrode (0.197 V versus NHE). In the concentric cell, the inner diameter of the tube containing CCl_4 and the $\text{RuO}_2\text{-TiO}_2\text{/C}$ electrode is 2.0 mm, the thickness of the porous carbon electrode is 1.0 mm, the distance between the counter and working electrodes is 3.0 mm, and the thickness of the counter electrode is 3.0 mm. The height of the cell is 2.0 cm, and the volume capacity of the cell is around 2.0 mL. The total volume of the CCl_4 reservoir is 6.0 mL, and the total volume of the $\text{NaCl/H}_2\text{O}$ reservoir is 2.0 mL. The CV measurements were carried out on a CHI660B electrochemical workstation. The galvanostatic charge and discharge profiles were obtained with an Arbin battery test station.

Material characterizations. Scanning electron microscopy (SEM) images were taken with Hitachi SU-70 analytical SEM (Japan). Powder X-ray diffraction (PXRD) data were collected on a Bruker D8 X-ray diffractometer using $\text{Cu K}\alpha$ radiation ($\lambda = 1.5418 \text{ \AA}$). Raman spectroscopy was performed on a Horiba Jobin Yvon Labram Aramis using a 532 nm diode-pumped solid-state laser, attenuated to give $\sim 900 \mu\text{W}$ power at the sample surface. Viscosity Measurements were carried out using a CANNON-FENSKE viscometer.

Energy density calculations. The energy density of CFB was calculated based on the 600 mAh cell used in this study with Eq. (1). The average operating potential is 1.8 V at 10 mA/cm², the volume of CCl_4 is 6.0 mL, the volume of $\text{NaCl/H}_2\text{O}$ is 2.0 mL and the volume of $\text{Na}(\text{Ti}_2(\text{PO}_4)_3)$ is 0.592 mL (weight = 5.0 g, density = 2.96 g/mL, volume = 2.96 g/mL \div 5.0 g = 0.592 mL). The total volume of active materials is 8.592 mL. Based on these configurations, the cell-level energy density (based on active materials) is 125.7 Wh/L.

$$\text{Energy density} = \frac{\text{Cell capacity} \times \text{average potential}}{\text{Total volume of active materials}} \quad (1)$$

Data availability

The data that support the findings within this paper are available within the article and Supplementary Information. Additional data are available from the corresponding authors upon request. Source data are provided with this paper.

Received: 14 January 2021; Accepted: 8 February 2022;

Published online: 11 March 2022

References

- Yang, Z. et al. Electrochemical energy storage for green grid. *Chem. Rev.* **111**, 3577–3613 (2011).
- Ansari, M. I. H., Qurashi, A. & Nazeeruddin, M. K. Frontiers, opportunities, and challenges in perovskite solar cells: a critical review. *J. Photochem. Photobiol. C* **35**, 1–24 (2018).
- Lu, X., McElroy, M. B. & Kiviluoma, J. Global potential for wind-generated electricity. *Proc. Natl Acad. Sci.* **106**, 10933–10938 (2009).
- Dunn, B., Kamath, H. & Tarascon, J.-M. Electrical energy storage for the grid: a battery of choices. *Science* **334**, 928–935 (2011).
- Ponce de Leon, C., Frias-Ferrer, A., Gonzalez-Garcia, J., Szanto, D. A. & Walsh, F. C. Redox flow cells for energy conversion. *J. Power Sources* **29**, 716–732 (2006).
- Soloveichik, G. L. Flow batteries: current status and trends. *Chem. Rev.* **115**, 11533–11558 (2015).
- Leung, P. et al. Progress in redox flow batteries, remaining challenges and their applications in energy storage. *RSC Adv.* **2**, 10125–10156 (2012).
- Viswanathan, V., Crawford, A., Reed, D., Thomsen, E.D. & Sprenkle, V. Chemistry agnostic cost performance model for redox flow batteries. DOE/OE Peer Review 2016 (2016).
- Tan, R. et al. Hydrophilic microporous membranes for selective ion separation and flow-battery energy storage. *Nat. Mater.* **19**, 195–202 (2020).
- Chai, J., Lashgari, A. & Jiang, J. Electroactive materials for next-generation redox flow batteries: from inorganic to organic. *ACS Symp. Series* **1364**, 1–47 (2020).
- Schwan, S. et al. Substituent pattern effects on the redox potentials of quinone-based active materials for aqueous redox flow batteries. *ChemSusChem* **13**, 5480–5488 (2020).
- Lee, W., Park, G. & Kwon, Y. Alkaline aqueous organic redox flow batteries of high energy and power densities using mixed naphthoquinone derivatives. *Chem. Eng. Sci.* **386**, 123985 (2020).
- Goulet, M.-A. et al. Extending the lifetime of organic flow batteries via redox state management. *J. Am. Chem. Soc.* **141**, 8014–8019 (2019).
- Hofmann, J. D. et al. Quest for organic active materials for redox flow batteries: 2,3-Diaza-anthraquinones and their electrochemical properties. *Chem. Mater.* **30**, 762–774 (2018).
- Kwabi, D. G. et al. Alkaline quinone flow battery with long lifetime at pH 12. *Joule* **2**, 1894–1906 (2018).
- Skyllas-Kazacos, M., Chakrabarti, M. H., Hajimolana, S. A., Mjalli, F. S. & Saleem, M. Progress in flow battery research and development. *J. Electrochem. Soc.* **158**, R55 (2011).
- Ulaganathan, M. et al. Recent advancements in all-vanadium redox flow. *Batteries. Adv. Mater. Inter.* **3**, 1500309 (2016).
- Wei, X. et al. Materials and systems for organic redox flow batteries: status and challenges. *ACS Energy Lett.* **2**, 2187–2204 (2017).
- Darling, R. M., Gallagher, K. G., Kowalski, J. A., Ha, S. & Brushett, F. R. Pathways to low-cost electrochemical energy storage: a comparison of aqueous and nonaqueous flow batteries. *Energy Environ. Sci.* **7**, 3459–3477 (2014).
- Janoschka, T. et al. An aqueous, polymer-based redox-flow battery using non-corrosive, safe, and low-cost materials. *Nature* **527**, 78–81 (2015).
- Duduta, M. et al. Semi-solid lithium rechargeable flow battery. *Adv. Energy Mater.* **1**, 511–516 (2011).
- Hamelet, S. et al. Non-aqueous Li-based redox flow batteries. *J. Electrochem. Soc.* **159**, A1360–A1367 (2012).
- Hine, F. & Yasuda, M. Studies on the Moor of the chlorine electrode process. *J. Electrochem. Soc.* **121**, 1289 (1974).
- Janssen, L. J. J., Starmans, Li. M. C., Visser, J. G. & Barendrecht, E. Mechanism of the chlorine evolution on a ruthenium oxide/titanium oxide electrode and on a ruthenium electrode. *Electrochim. Acta* **22**, 1093–1100 (1977).
- Agarwal, H., Florian, J., Goldsmith, B. R. & Singh, N. $\text{V}^{2+}/\text{V}^{3+}$ redox kinetics on glassy carbon in acidic electrolytes for vanadium redox flow batteries. *ACS Energy Lett.* **4**, 2368–2377 (2019).
- U.S. Geological Survey. Salt Statistics and Information. <https://www.usgs.gov/centers/national-minerals-information-center/salt-statistics-and-information/> (2022)
- Moorhouse, J. *Modern Chlor-alkali Technology*, vol. 8 (John Wiley & Sons, 2008).
- Winter, L. & Degner, G. *Minute Epics Of Flight (Grosset & Dunlap, 1933)*.
- Kim, J. T. & Jorne, J. The kinetics of a chlorine graphite electrode in the zinc-chlorine battery. *J. Electrochem. Soc.* **124**, 1473–1477 (1977).
- Kim, J. T. & Jorne, J. Mass transfer of dissolved chlorine to a rotating-zinc hemisphere in ZnCl_2 solution. *J. Electrochem. Soc.* **125**, 89–94 (1978).
- Jorne, J., Kim, J. T. & Kralik, D. The zinc-chlorine battery: half-cell overpotential measurements. *J. Appl. Electrochem.* **9**, 573–579 (1979).
- Kim, J. T. & Jorne, J. The kinetics and mass transfer of zinc electrode in acidic zinc-chloride solution. *J. Electrochem. Soc.* **127**, 8–15 (1980).
- Thomas, D. L. A LiAl/Cl_2 battery with a four-component alkali-metal chloride electrolyte. *J. Electrochem. Soc.* **136**, 3553 (1989).
- Holleck, G. L. The reduction of chlorine on carbon in $\text{AlCl}_3\text{-KCl-NaCl}$ melts. *J. Electrochem. Soc.* **119**, 1158 (1972).
- Gifford, P. R. & Palmisano, J. B. An aluminum/chlorine rechargeable cell employing a room temperature molten salt electrolyte. *J. Electrochem. Soc.* **135**, 650 (1988).
- Hooley, J. G. A search for intercalation in the graphite-chlorine system. *Carbon* **8**, 333–339 (1970).
- Young, C. L. Sulfur dioxide. Chlorine, fluorine and chlorine oxides. *Sol. Data Ser.* **12**, 333–445 (1983).
- Li, L. et al. A stable vanadium redox-flow battery with high energy density for large-scale energy storage. *Adv. Energy Mater.* **1**, 394–400 (2011).
- Li, X. et al. Investigation of electrolytes of the vanadium redox flow battery (VII): Prediction of the viscosity of mixed electrolyte solution ($\text{VOSO}_4 + \text{H}_2\text{SO}_4 + \text{H}_2\text{O}$) based on Eyring's theory. *J. Chem. Thermodyn.* **134**, 69–75 (2019).
- Denton, D. A., Harrison, J. A. & Knowles, R. I. Chlorine evolution and reduction on $\text{RuO}_2/\text{TiO}_2$ electrodes. *Electrochim. Acta* **24**, 521–527 (1979).
- Exner, K. S., Anton, J., Jacob, T. & Over, H. Controlling selectivity in the chlorine evolution reaction over RuO_2 -based catalysts. *Angew. Chem. Int. Ed.* **53**, 11032–11035 (2014).
- Zeradjanin, A. R., Menzel, N., Schuhmann, W. & Strasser, P. On the faradaic selectivity and the role of surface inhomogeneity during the chlorine evolution reaction on ternary Ti–Ru–Ir mixed metal oxide electrocatalysts. *Phys. Chem. Chem. Phys.* **16**, 13741–13747 (2014).
- Karlsson, R. K. B. & Cornell, A. Selectivity between oxygen and chlorine evolution in the chlor-alkali and chlorate processes. *Chem. Rev.* **116**, 2982–3028 (2016).
- Arora, P. & Zhang, Z. Battery separators. *Chem. Rev.* **104**, 4419–4462 (2004).
- Nguyen, T. & Savinell, R. F. Flow batteries. *Electrochem. Soc. Interface* **19**, 54–56 (2010).

46. Lin, K. et al. Alkaline quinone flow battery. *Science* **349**, 1529–1532 (2015).
47. Bosse, D. & Bart, H.-J. Viscosity calculations on the basis of Eyring's absolute reaction rate theory and COSMOSPACE. *Ind. Eng. Chem. Res.* **44**, 8428–8435 (2005).
48. Lewis, J. R. The viscosity of liquids containing dissolved gases. *J. Am. Chem. Soc.* **47**, 626–640 (1925).
49. Xu, Q., Zhao, T. S. & Zhang, C. Effects of SOC-dependent electrolyte viscosity on performance of vanadium redox flow batteries. *Appl. Energy* **130**, 139–147 (2014).
50. Sun, C., Chen, J., Zhang, H., Han, X. & Luo, Q. Investigations on transfer of water and vanadium ions across Nafion membrane in an operating vanadium redox flow battery. *J. Power Sources* **3**, 890–897 (2010).
51. Song, Y., Li, X., Yan, C. & Tang, A. Unraveling the viscosity impact on volumetric transfer in redox flow batteries. *J. Power Sources* **456**, 228004 (2020).
52. Bard, A. J., Faulkner, L. R., Leddy, J., Zoski, C. G. *Electrochemical Methods: Fundamentals And Applications*, vol. 2 (Wiley, 1980).
53. Vitagliano, V. & Lyons, P. A. Diffusion coefficients for aqueous solutions of sodium chloride and barium chloride. *J. Am. Chem. Soc.* **78**, 1549–1552 (1956).
54. Tang, A. & Sandall, O. C. Diffusion coefficient of chlorine in water at 25–60 °C. *J. Chem. Eng. Data* **30**, 189–191 (1985).
55. Hildebrand, J. H. & Lamoreaux, R. H. Diffusivity of gases in liquids. *Proc. Natl Acad. Sci.* **71**, 3321–3324 (1974).
56. Aaron, D., Tang, Z., Papandrew, A. B. & Zawodzinski, T. A. Polarization curve analysis of all-vanadium redox flow batteries. *J. Appl. Electrochem.* **41**, 1175 (2011).
57. Butler, P. C., Eidler, P. A., Grimes, P. G., Klassen, S. E., Miles, R. C. Zinc/bromine batteries. Handbook of Batteries, 39, 3rd ed., McGraw Hill (McGraw Hill, 2001).
58. Cathro, K. J. Performance of zinc/bromine cells having a propionitrile electrolyte. *J. Power Sources* **23**, 365–363 (1988).
59. Wang, H. et al. Novel aqueous Li⁺ (or Na⁺)/Br⁻ hybrid-ion battery with super high areal capacity and energy density. *J. Mater. Chem. A* **7**, 13050–13059 (2019).
60. Scott, T. M. The suitability of mineral oil as a halogen extraction solvent. *J. Chem. Educ.* **68**, 950 (1991).
61. U.S. Department of Energy. AEP-A-E's 19 New Projects Focus on Battery Management and Storage. Target price for flow battery. <https://www.energy.gov/articles/arpa-e-s-19-new-projects-focus-battery-management-and-storage/> (2012).
62. The Chlorine Institute. Incident Statistics. <https://www.chlorineinstitute.org/transportation/incident-statistics/> (2021).
63. U.S. Department of labor, Occupational Safety and Health Administration. Permissible Exposure Limits-Annotated Tables Z-1. <https://www.osha.gov/annotated-pels/table-z-1/> (2017).
64. Pamphlet 86 Recommendations to Chlor-Alkali Manufacturing Facilities for the Prevention of Chlorine Releases 6 edn, (The Chlorine Institute, 2016).
65. Kumar, S. et al. Room temperature highly sensitive chlorine sensor based on reduced graphene oxide anchored with substituted copper phthalocyanine. *Sens. Actuators B Chem.* **327**, 128925 (2021).

Acknowledgements

This work was supported by the US Department of Energy ARPA-E Grant DEAR0000389.

Author contributions

S.H., L.C., and Xiu.F. contributed equally to this work. S.H. and L.C. conceived the idea of a membrane-free chlorine flow battery. S.H. performed the numerical simulations and physicochemical measurements. L.C., Xiu.F., and Xiaotong.F. did the material synthesis and electrochemical measurements. X.J. performs the DFT calculations. S.H. and L.C. analyzed the results and wrote the manuscript. B.W., C.C., J.C., C.Y., W.W., and C.L. participated in the discussions. C.W. supervised all the studies.

Competing interests

The authors declare no competing interests.

Additional information

Supplementary information The online version contains supplementary material available at <https://doi.org/10.1038/s41467-022-28880-x>.

Correspondence and requests for materials should be addressed to Long Chen or Chunsheng Wang.

Peer review information *Nature Communications* thanks Yongchai Kwon, Carlos Ponce de León, and the other, anonymous, reviewer(s) for their contribution to the peer review of this work. Peer reviewer reports are available.

Reprints and permission information is available at <http://www.nature.com/reprints>

Publisher's note Springer Nature remains neutral with regard to jurisdictional claims in published maps and institutional affiliations.



Open Access This article is licensed under a Creative Commons Attribution 4.0 International License, which permits use, sharing, adaptation, distribution and reproduction in any medium or format, as long as you give appropriate credit to the original author(s) and the source, provide a link to the Creative Commons license, and indicate if changes were made. The images or other third party material in this article are included in the article's Creative Commons license, unless indicated otherwise in a credit line to the material. If material is not included in the article's Creative Commons license and your intended use is not permitted by statutory regulation or exceeds the permitted use, you will need to obtain permission directly from the copyright holder. To view a copy of this license, visit <http://creativecommons.org/licenses/by/4.0/>.

© The Author(s) 2022